Bioinspired micro/nanomotor with visible light energy–dependent forward, reverse, reciprocating, and spinning schooling motion

Jintao Tong[a,1], Dalei Wang[a,1], Ye Liu[a,1], Xin Lou[b,c], Jiwei Jiang[a], Bin Dong[a,2], Renfeng Dong[d,2], and Mingcheng Yang[b,c,e,2]

[a]Institute of Functional Nano & Soft Materials (FUNSOM), Jiangsu Key Laboratory for Carbon-Based Functional Materials & Devices and State and Local Joint Engineering Laboratory for Novel Functional Polymeric Materials, Soochow University, Suzhou, Jiangsu 215123, China; [b]Beijing National Laboratory for Condensed Matter Physics and Laboratory of Soft Matter Physics, Institute of Physics, Chinese Academy of Sciences, Beijing 100190, China; [c]School of Physical Sciences, University of Chinese Academy of Sciences, Beijing 100049, China; [d]School of Chemistry, South China Normal University, Guangzhou 510006, China; and [e]Songshan Lake Materials Laboratory, Dongguan, Guangdong 523808, China

Edited by David A. Weitz, Harvard University, Cambridge, MA, and approved September 4, 2021 (received for review March 9, 2021)

In nature, microorganisms could sense the intensity of the incident visible light and exhibit bidirectional (positive or negative) phototaxis. However, it is still challenging to achieve the similar biomimetic phototaxis for the artificial micro/nanomotor (MNM) counterparts with the size from a few nanometers to a few micrometers. In this work, we report a fuel-free carbon nitride (C_3N_4)/polypyrrole nanoparticle (PPyNP)-based smart MNM operating in water, whose behavior resembles that of the phototactic microorganism. The MNM moves toward the visible light source under low illumination and away from it under high irradiation, which relies on the competitive interplay between the light-induced self-diffusiophoresis and self-thermophoresis mechanisms concurrently integrated into the MNM. Interestingly, the competition between these two mechanisms leads to a collective bidirectional phototaxis of an ensemble of MNMs under uniform illuminations and a spinning schooling behavior under a nonuniform light, both of which can be finely controllable by visible light energy. Our results provide important insights into the design of the artificial counterpart of the phototactic microorganism with sophisticated motion behaviors for diverse applications.

light-driven micromotor | phototaxis | self-diffusiophoresis | self-thermophoresis | collective behavior

In nature , many microorganisms can respond to light and exhibit phototaxis. For instance, green algae can be attracted by weak light and escape from strong light (1–3). Inspired by nature, great efforts have been exerted to develop artificial light–driven and photoresponsive micro/nanomotors (MNMs) (4–8). During the last decade, significant progresses have been made in almost all aspects of the light-driven MNM (9–11). Until now, several different propulsion mechanisms have been established in order to propel the MNMs by light. The efficient propulsion can be realized based on bubbles generated through the photoirradiation-enhanced catalytic reaction (12) or the photoisomerization reactions (13, 14). It can also be achieved based on the Marangoni forces originating from the surface tension gradient caused by the photodoping process or the surfactant released from the photodegraded-light–responsive polymer (15). Recently, tailor-designed external fuel-free light-powered MNMs have been reported, whose propulsion can be achieved via self-diffusiophoresis induced by the photocatalytic reaction (16, 17) or the self-thermophoresis caused by the photothermal effect (18–20).

Light (ultraviolet [UV], visible [Vis], or near infrared [NIR], etc.) (21–23) shows great versatility in manipulating the MNM's movement (including speed and direction) through adjusting its "on" and "off," wavelength, intensities, etc. (24–27). As a result, light cannot only govern the MNM trajectory in a programmable fashion by changing its incident direction but also enable the independent addressing of specific MNMs (28). These, together with the easily obtainable and remotely controllable features, make the light-driven MNM potentially attractive for various practical applications ranging from the controlled cargo capture, transportation, and release (29), cancer therapy (30), to dynamic assembly (31) or the environmental remediation (32). However, despite these progresses, for the light-driven MNMs, it is still challenging to realize the biomimetic bidirectional phototactic behaviors in water (i.e., positive phototaxis under weak light and negative phototaxis under strong light), as experienced by green algae. Intuitively, a bidirectionally phototactic MNM may be designed by combining two competitive light-driven mechanisms that are both photoresponsive, which could provide additional degree of freedom for motion regulation. Indeed, a 300-μm droplet has recently been reported to have the capability of bidirectional phototaxis in spiropyran's oil solution (33), which explored the effect of interfacial tension change caused by the spiropyran photoisomerization and the photothermal effect. However, this active droplet cannot be miniaturized to the size of MNM

Significance

Light intensity–dependent bidirectional phototaxis is vital for microorganisms (e.g., green algae) to gain energy or escape from damage. Inspired by nature, artificial phototactic micro/nanomotors (MNMs) have been developed, which cannot only serve as perfect model systems for nonequilibrium physics but have great potentials in microfluidics and biomedical applications. However, unlike the biological microorganisms that possess the bidirectional phototactic capability by natural evolution, it is still challenging for the artificial MNMs to realize the similar biomimetic phototaxis, which greatly limits their applicability. Here, we innovatively combine the self-diffusiophoresis and self-thermophoresis mechanisms to achieve a visible light–driven MNM, exhibiting bidirectional phototaxis and intriguing light-controlled collective behaviors. These findings thus constitute an important step toward developing biomimetic photoresponsive active systems.

Author contributions: B.D. and M.Y. designed research; J.T., D.W., Y.L., and X.L. performed research; J.T., D.W., Y.L., X.L., J.J., B.D., R.D., and M.Y. analyzed data; and J.T., D.W., Y.L., B.D., and M.Y. wrote the paper.

The authors declare no competing interest.

This article is a PNAS Direct Submission.

[1]J.T., D.W., and Y.L. contributed equally to this work.

[2]To whom correspondence may be addressed. Email: bdong@suda.edu.cn, rfdong@m.scnu.edu.cn, or mcyang@iphy.ac.cn.

This article contains supporting information online at http://www.pnas.org/lookup/suppl/doi:10.1073/pnas.2104481118/-/DCSupplemental.

Published October 15, 2021.

ranging from a few nanometers to a few micrometers (colloidal motor) (34) because its self-propelling velocity sharply decays when reducing its size, which largely limits its application in precision surgery and biomedicine, etc., where MNMs are necessary (25). The demanding medium (spiropyran's oil solution) where the active droplet operates also confines its performance to a special environment. In addition, the active droplet is unstable due to the droplet fusion, making it unsuitable for the investigation of the fascinating light-controlled collective behaviors of active matter. Therefore, it is very desirable to develop new mechanisms to achieve robust and fuel-free MNMs (active colloids) with the light intensity–dependent bidirectional phototaxis.

In this work, we report a fuel-free visible light–driven MNM, which is capable of sensing the light intensity changes and exhibits the biomimetic individual or collective bidirectional phototaxis based on the combined self-diffusiophoresis and self-thermophoresis mechanisms. This MNM consists of binary active components: photocatalytic carbon nitride (C_3N_4) (35) and photothermal polypyrrole nanoparticle (PPyNP) (36). The competition between the local chemical (i.e., self-diffusiophoresis) and thermal (i.e., self-thermophoresis) gradients self-generated due to the photohydrolysis catalyzed by C_3N_4 and the light-absorbing PPyNP, accounts for the light energy–dependent motions. More interestingly, by tuning the light energy, the interplay between the two competitive mechanisms leads to the appearance of the unique reciprocating movement of a single MNM and the emergence of the spinning schooling behavior for a group of MNMs. We believe the unique and versatile motion behaviors of the current MNM can further advance the design and development of the artificial counterpart of the phototactic microorganism for various practical applications.

Results and Discussion

The MNM consisting of PPyNP, C_3N_4, and the gelatin excipient is fabricated by the emulsion solvent evaporation technique (32); more detailed descriptions are shown in *SI Appendix*, section S2 (*SI Appendix*). The MNM is spherical in shape and has a size of around 3 μm (*Inset* in Fig. 1*B*). Unless otherwise stated, we utilize a parallel beam of light in experiments in order to exclusively study the effect of the light intensity on the motion behavior of the MNM, as shown in *SI Appendix*, Figs. S5 and S6. The current C_3N_4/PPyNP-based MNM can sense the irradiation intensity changes and exhibit visible light energy–dependent motion behavior. Under a weak light irradiation with an intensity of 0.4 W/cm^2, the MNM shows the positive phototaxis and moves toward light with a velocity of around 5.5 μm/s, as indicated in the schematic illustration (Fig. 1*A*), the movement trajectory (Fig. 1*B*), and the corresponding movie (Movie S1). When exposed to a strong light with an intensity of 1.2 W/cm^2, the MNM exhibits the negative phototaxis, namely it moves away from the light source with a velocity of around 8.0 μm/s (Fig. 1 *C* and *D* and Movie S1). There is a threshold of light intensity (i.e., 0.8 W/cm^2) at which the MNM only exhibits a Brownian-like motion (Fig. 1 *E* and *F* and Movie S1). This light energy–dependent motion resembles the phototactic behavior of single green algae under different irradiation intensities (Movie S2). Thus, the C_3N_4/PPyNP-based colloidal particle constitutes a genuine biomimetic phototactic MNM (active colloid). More intriguingly, we find out that the current C_3N_4/PPyNP-based MNM even exhibits a unique reciprocating motion by simply adjusting the light energy during its motion process. As can be seen from Fig. 1 *G* and *H* and Movie S1, the MNM first moves toward the light source under weak irradiation (0.4 W/cm^2). After 4 s, as the light energy is increased to 1.2 W/cm^2, the MNM slowly decelerates, stops, then changes its moving direction and moves away from the light source. This reciprocating motion can be repeated multiple times, as illustrated in the position displacement in *SI Appendix*, Fig. S7. The present reciprocating motion is realized by solely adjusting the light energy, which is in stark contrast to the previous studies that require the change of the light source position to achieve similar movement (22), thus extremely simplifying the motion control strategy and having great potentials for practical applications.

Besides the self-propelled direction, the motion speed of the C_3N_4/PPyNP-based MNM is also significantly dependent on the incident light energy (Fig. 2*A*). Positive phototaxis appears

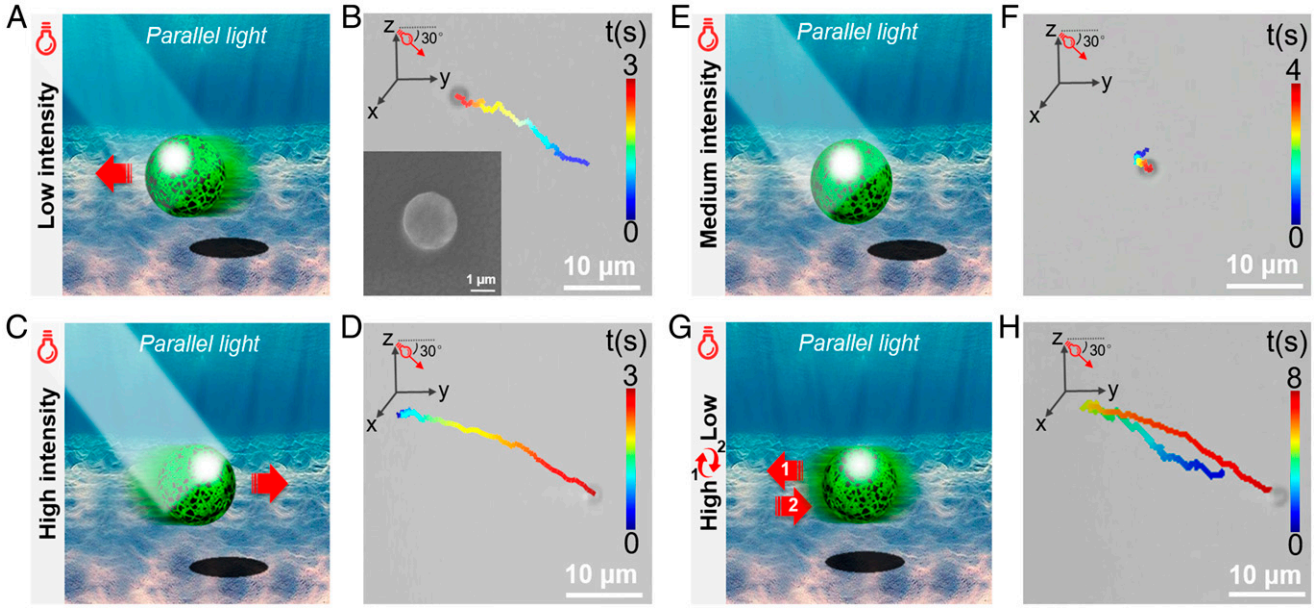

Fig. 1. Schematic illustration and the corresponding representative trajectory image obtained from Movie S1 showing the (*A, B*) positive phototaxis, (*C, D*) negative phototaxis, and (*E, F*) Brownian-like motion under weak (0.4 W/cm^2), strong (1.2 W/cm^2), and medium light (0.8 W/cm^2), respectively. *Inset* in (*B*): the SEM image of the C_3N_4/PPyNP-based MNM. (*G*) Schematic illustration and (*H*) the representative trajectory image obtained from Movie S1 showing the reciprocating motion of the C_3N_4/PPyNP-based MNM when adjusting the irradiation light intensity. The light is applied from the left side with the incident light angle of 30°.

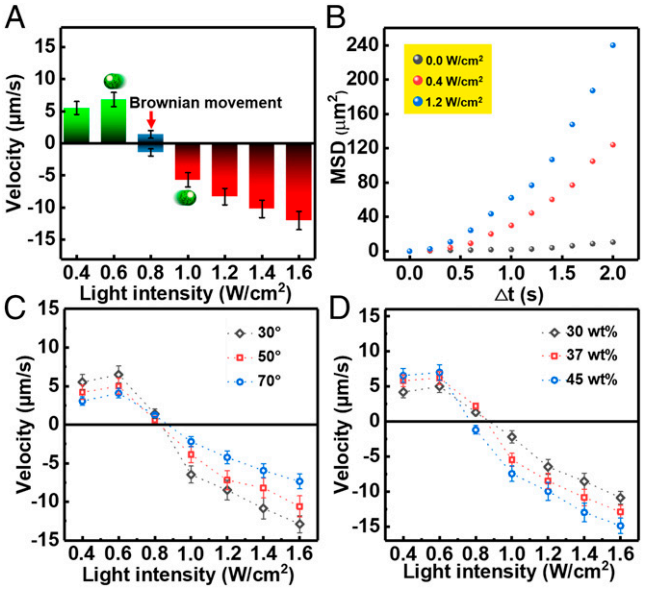

Fig. 2. (*A*) Self-propelling velocity of the MNM as a function of light intensity (Error bars denote the SD). Here, the negative phototaxis velocity is defined as negative. (*B*) Mean square displacement of the MNM under different light intensities (0, 0.4, and 1.2 W/cm^2). The speed of positive and negative phototaxis of the C_3N_4/PPyNP-based MNM as a function of the light intensity, with (*C*) different incident angles (30°, 50°, and 70°) and (*D*) different C_3N_4 contents inside the MNM (30, 37, and 45 wt%).

under 0.4- to 0.8-W/cm^2 irradiation with movement speed increasing at first (under 0.4- to 0.6-W/cm^2 illumination) followed by decreasing (under 0.6- to 0.8-W/cm^2 light) (Fig. 2*A*). Note that the self-propulsion trivially vanishes under very weak illumination power. Negative phototaxis appears when the MNM senses an illumination stronger than 0.8 W/cm^2, and its speed monotonically increases with the irradiation intensity (Fig. 2*A*). Additionally, the self-propelled motion in the case of both positive and negative phototaxis is reflected in the mean square displacement of the MNMs plotted in Fig. 2*B*. Moreover, the light illumination angle has a large influence on the MNM's speed (Fig. 2*C*); namely, the moving velocity decreases with the increasing incident light angle in the case of both positive and negative phototaxis (the MNM basically self-propels in the x-y plane, with a distance from the substrate of about 2 μm). This is simply because the light intensity in the x-y plane decreases with increasing the illumination angle. In contrast, the phototactic speed of the MNM enhances as the concentration of the active components (C_3N_4 to PPyNP ratio equals to 1) increases, as expected (Fig. 2*D*). Note that the minimum concentration of gelatin excipient inside the MNM has to be at least 10% weight percentage (10 wt%) to obtain the spherical MNM.

The unprecedented light energy–dependent phototaxis in water presumably originates from the unique properties of the two active constituent parts of the current MNMs (i.e., C_3N_4 and PPyNP). On the one hand, the positive phototaxis is due to the self-diffusiophoresis (Fig. 3*A*). C_3N_4 is a well-known inorganic polymeric photocatalyst, which is capable of hydrolyzing water based on the photocatalytic reaction (35).

$$C_3N_4 + h\nu \rightarrow e^- + h^+ \quad [1]$$

$$O_2 + e^- \rightarrow \bullet O_2^- \quad [2]$$

$$H_2O + h^+ \rightarrow H^+ + \bullet OH. \quad [3]$$

Under light irradiation, charge separation occurs on C_3N_4 (Eq. 1), and the electrons are injected into PPyNP (37). The charge separation process between C_3N_4 and PPyNP is confirmed by the generated photocurrent shown in *SI Appendix*, Fig. S8 and section S5. The presence of PPyNP can enhance the electron–hole separation efficiency of the C_3N_4 as evidenced by the longer fluorescence lifetimes (about 1.7 times longer as compared to that of the pristine C_3N_4; *SI Appendix*, Fig. S9 and section S5). The electrons react with O_2 inside the solution, leading to the formation of superoxide radical ($\bullet O_2^-$) (Eq. 2), while the holes react with water, resulting in proton (H^+) and hydroxyl radical ($\bullet$OH) (Eq. 3). The generation of the proton and $\bullet O_2^-$ are confirmed by the pH indicator (Fig. 3 *B* and *C* and *SI Appendix*, section S6) and the (5, 5-Dimethyl-1-pyridine-N-oxid) spin-trapping electron paramagnetic resonance (EPR) technique (*SI Appendix*, Fig. S11 and section S7), respectively. Different ionic species have different diffusivities, with the protons exhibiting the largest diffusion rate. As a consequence, a local electrical field is established (as can be seen from the simulation in Fig. 3*D* and *SI Appendix*, section S8), and the MNM, which has the negative charge on its surface (*SI Appendix*, Fig. S13 and section S9), is thus propelled toward the light source by this electrical field based on the self-diffusiophoresis mechanism (Fig. 3*D*) (38, 39). We emphasize that the present MNM is an isotropic sphere instead of Janus particle, and the symmetry breaking required by the self-propulsion arises from the shading effect of the MNM. Furthermore, the self-propelling speed of the MNM decreases with the increase of the electrolyte (i.e., NaCl) concentration (*SI Appendix*, Fig. S14 and section S10), further supporting the proposed mechanism (40).

On the other hand, the negative phototaxis motion originates from the self-thermophoresis, caused by the photothermal effect of PPyNP component owing to its broad light absorption band in the visible range and the light-to-heat conversion capability (41), which can be seen from the temperature increase of the solution containing MNMs under light illumination as shown in Fig. 3 *F* and *G* and *SI Appendix*, section S11. Since the light is directional and the MNM is nontransparent (the shading effect, Fig. 3*E*), it is the irradiated side that has higher temperature, thus leading to a local temperature gradient across the MNM. The temperature profile surrounding the MNM is calculated through the Laplace equation in the form of $T(r) \propto 1/r$ (42), where r is the distance from to the MNM center. As shown in Fig. 3*H* and *SI Appendix*, section S12, the temperature at the liquid–MNM interface is enhanced owing to the photothermal effect, and the temperature decreases gradually across the MNM due to the weak thermal conductance of the composite comprising the MNM (43), which is consistent with the literature (18). The self-thermophoretic force F_T is proportional to the self-generated local thermal gradient (19):

$$F_T = -\alpha_T k_B \nabla T, \quad [4]$$

where K_B is the Boltzmann factor, ∇T the temperature gradient, and α_T the thermal diffusion factor. In most situations, α_T is positive, such that the self-thermophoretic force is against the thermal gradient. The temperature gradient thus drives the negative phototactic motion of the C_3N_4/PPyNP-based MNM.

However, under light irradiation, both self-diffusiophoresis and self-thermophoresis occur and they can compete with each other. To better elucidate the motion mechanism of the MNM, we have conducted the control experiments. We have separately prepared PPyNP/polyvinyl alcohol (PVA)-based MNM and C_3N_4/PtNP-based MNM as the models to quantify the self-thermophoretic and self-diffusiophoresis forces, respectively. Among others, the motion of the PPyNP/PVA-based MNM solely relies on the self-thermophoresis mechanism, as shown in Movie S3 (detailed discussion is shown in *SI Appendix*, Figs. S16–S18 and section S13); while the self-propulsion of the C_3N_4/PtNP-based MNM is exclusively based on self-diffusiophoresis, as shown in Movie S3

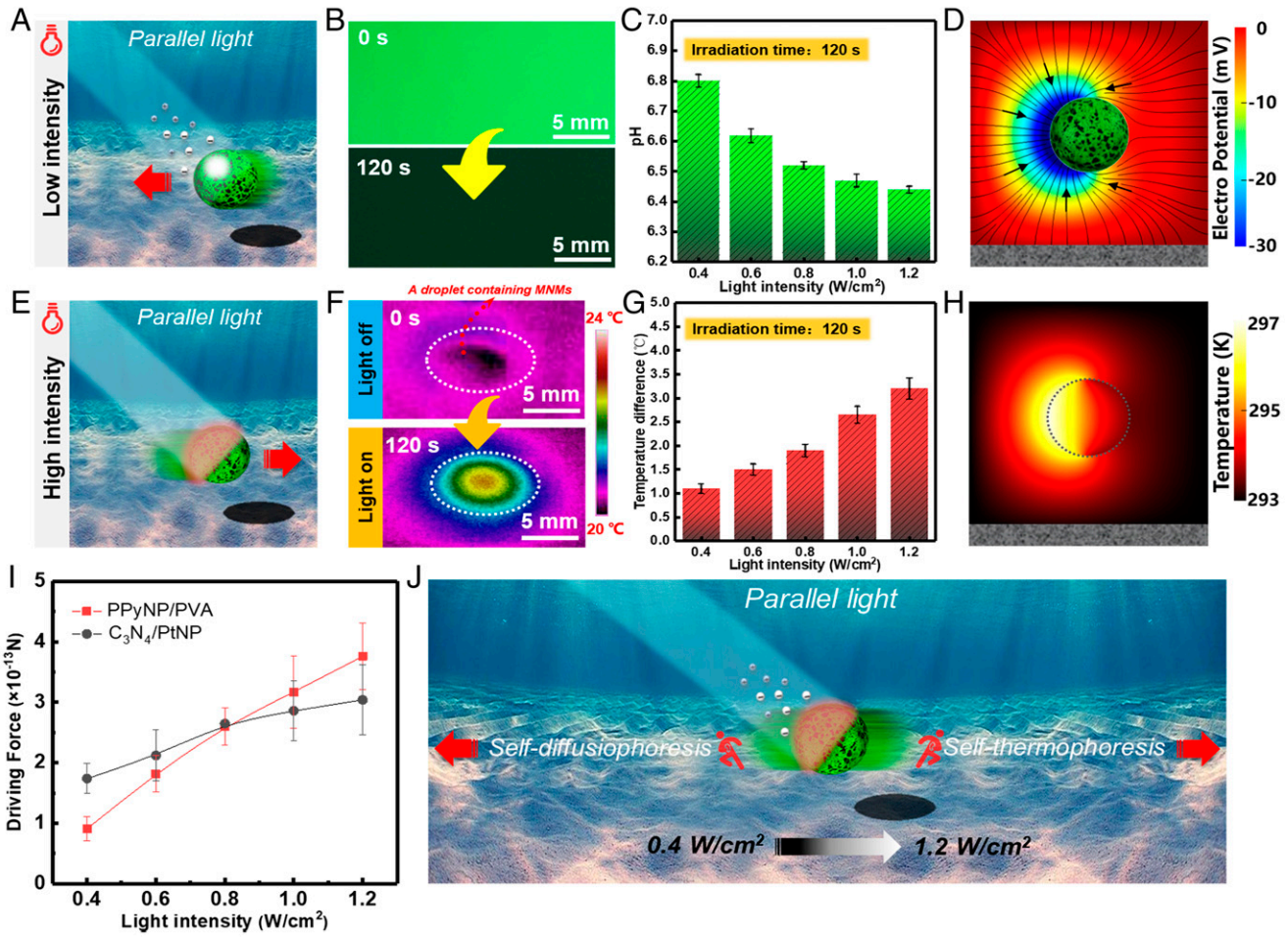

Fig. 3. (*A*) Schematic illustration showing the self-diffusiophoresis mechanism under weak light irradiation. (*B*) Fluorescence image of the solution containing the MNM and pyranine pH indicator before and after 0.4-W/cm^2 light irradiation for 2 min. (*C*) Relationship between pH of the solution containing the MNM (1.5×10^2/μL) and the irradiation intensity. (*D*) Simulation showing the distribution of the electric potential surrounding the MNM under light irradiation. (*E*) Schematic illustration showing the self-thermophoresis mechanism under strong light irradiation. (*F*) Infrared thermal images showing the droplet containing the MNM (1.5×10^2/μL) before and after 1.2-W/cm^2 light irradiation for 2 min. (*G*) The temperature difference of the droplet containing the MNM before and after light irradiation with different light energy. (*H*) Simulation showing the temperature distribution surrounding the MNM under light irradiation. (*I*) The driving force magnitudes of the PPyNP/PVA-based MNM and the C_3N_4/PtNP-based MNM at different light intensities. (*J*) Schematic illustration showing the interplay between the self-diffusiophoresis and self-thermophoresis mechanisms under different light intensity. Error bars in *C*, *G*, and *I* denote the SD.

(detailed discussion is shown *SI Appendix*, Figs. S19–S21 and section S14). We have recorded the self-propelling velocities of these two MNMs under different light energy (*SI Appendix*, Fig. S22 and section S15) and estimated the corresponding driving force F_d by utilizing the Stokes equation (44):

$$F_d = 6\pi\eta RU, \quad [5]$$

where η refers to the water viscosity (9×10^{-4} Pa · s at room temperature), R to the radius of the MNM (1.4 μm), and U to the self-propelling velocity.

Since ∇T is proportional to the light power (18), the thermophoretic force on the PPyNP/PVA-based MNM is proportional to the light intensity, as can be seen from Fig. 3*I* (red curve). On the other hand, the diffusiophoretic force on the C_3N_4/PtNP-based MNM also changes with the light intensity, which can be explained in terms of the expression of the self-diffusiophoretic velocity (38):

$$U = \frac{\varepsilon}{4\pi\eta}\frac{K_BT}{eZ}\left\{\beta\zeta - 2\frac{K_BT}{eZ}ln\left[1-\left(tan\frac{eZ\zeta}{2K_BT}\right)^2\right]\right\}\nabla ln\, C\,, \quad [6]$$

with C being the concentration of the photocatalytic reaction product, ε the permittivity, e the elementary charge, Z the charge of the ion, and ζ the zeta potential. There is a logarithmic relationship between the self-diffusiophoretic velocity of the MNM and the local concentration gradient of the photocatalytic product that is proportional to the irradiation intensity (45). This relation correlates well with our experimental observations (Fig. 3*I*, black curve). Notably, there is an intersection between the two curves at the light intensity around 0.8 W/cm^2 (Fig. 3*I*), below which the self-diffusiophoretic force dominates, otherwise the self-thermophoretic force dominates. At the point of intersection, the self-diffusiophoretic and self-thermophoretic forces roughly balance each other (Fig. 3*J*). These results agree well with the observations in Fig. 1, more detailed descriptions can be seen in *SI Appendix*, section S15. It can thus be concluded that the two mechanisms (i.e., self-diffusiophoresis and self-thermophoresis) coexist, and it is the dominant mechanism that determines the motion behavior of the C_3N_4/PPyNP-based MNM.

A group of MNMs show collective positive, negative phototaxis, or Brownian-like motion (*SI Appendix*, Fig. S25 *A–F* and

Movie S4) under 0.4-, 1.2-, and 0.8-W/cm^2 irradiation, respectively (the light incident angle is 30° in all cases), with similar velocities to those in the case of the single MNM (*SI Appendix*, Fig. S25*G*). The light energy–dependent collective phototaxis resembles that of the green algae (Movie S5). The mechanisms behind the collective phototaxis are similar to those behind the single MNM motion (i.e., the competitive self-diffusiophoresis and self-thermophoresis). Note that more-photocatalytic reaction products and more-significant thermal effect are generated in the case of the MNM swarms, as evidenced by the lower solution pH and larger temperature increase under the same light energy (*SI Appendix*, Figs. S25*H*, S26, and S27). The collective phototaxis can also be observed at the macroscopic scale. As can be seen from Movie S6 and *SI Appendix*, section S17, the C_3N_4/PPyNP-based MNMs move toward or away from the side wall of the quartz cuvette, where the light source is placed separately with low- (0.4 W/cm^2) or high-intensity (1.2 W/cm^2) illumination.

Since the light intensity directly determines the phototactic behavior of the present MNM, interesting phenomenon could be expected if we employed a nonuniform divergent light beam having a wide range of the intensity that covers 0.8 W/cm^2 (positive phototaxis, Brownian-like motion, and negative phototaxis can all happen in the same field of view). Under the divergent beam of light with 1.0 W/cm^2 (the light intensity emitted from the light source), the local light intensity–dependent phototaxis leads to a unique spinning schooling behavior of the MNMs (with the concentration of 2 × 10^5/μL and the incident light angle of 30°, more details are shown in *SI Appendix*, section S18), which resembles the schooling behavior of fish, as illustrated in the Fig. 4 *A* and *B* and Movie S7. The MNMs close to the vortex center (Fig. 4*C*, black curve) move in circles with a low speed of around 3 μm/s. The MNMs' speed increases with the increasing distance to the vortex center (Fig. 4*D*) and reaches ∼8 μm/s at the vortex periphery (Fig. 4*C*, green curve). The spinning collective behavior emerges only under a moderate light intensity emitted from the light source (roughly between 1.0 and 1.2 W/cm^2). Under weak and strong light, the MNMs separately exhibit collective positive and negative phototaxis, as demonstrated in Movie S8. Moreover, the collective spinning motion can entrain immersed passive particles, as evidenced by the fact that the passive polystyrene (PS) tracer microparticles (electrically neutral) exhibit the similar spinning schooling behavior when mixed with the MNMs (Movie S9).

To further understand the mechanism underlying the spinning collective behavior, the light intensity distribution is roughly estimated based on the vortex size and the profile of the divergent light intensity (*SI Appendix*, section S18). The local light intensity gradually decreases as the distance increases from the light beam center, the MNM at position 1 in Fig. 4*E* (which is very close to the light beam center, thus senses a light intensity similar to that of the light source) experiences a light intensity of ∼1.0 W/cm^2 and exhibits the negative phototaxis. At position 3, the MNM shows the positive phototaxis because the local light intensity in this area is around 0.6 W/cm^2. At position 2 in Fig. 4*E*, where the local light intensity is around 0.8 W/cm^2, the MNM exhibits a Brownian-like motion. Moreover, the light beam can loosely trap the MNMs as the MNMs near the beam periphery move toward the beam center due to the positive phototaxis and interparticle diffusiophoretic interactions. Consequently, the ensemble of MNMs effectively experiences a clockwise torque (equivalent to a local shear) and hence spins clockwise in a collective manner. Furthermore, a coarse-grained dynamics simulation has been performed to reproduce the spinning schooling behavior of the MNMs (detailed in *SI Appendix*, section S19), in which the light intensity–dependent self-propulsion is essentially taken into account. The simulation result is well consistent with the experimental observation (Fig. 4*F* and Movie S10).

Conclusion

We report a C_3N_4/PPyNP-based MNM which can sense the light intensity change and act bidirectionally. Owing to the photocatalytic property of C_3N_4 and the photothermal effect

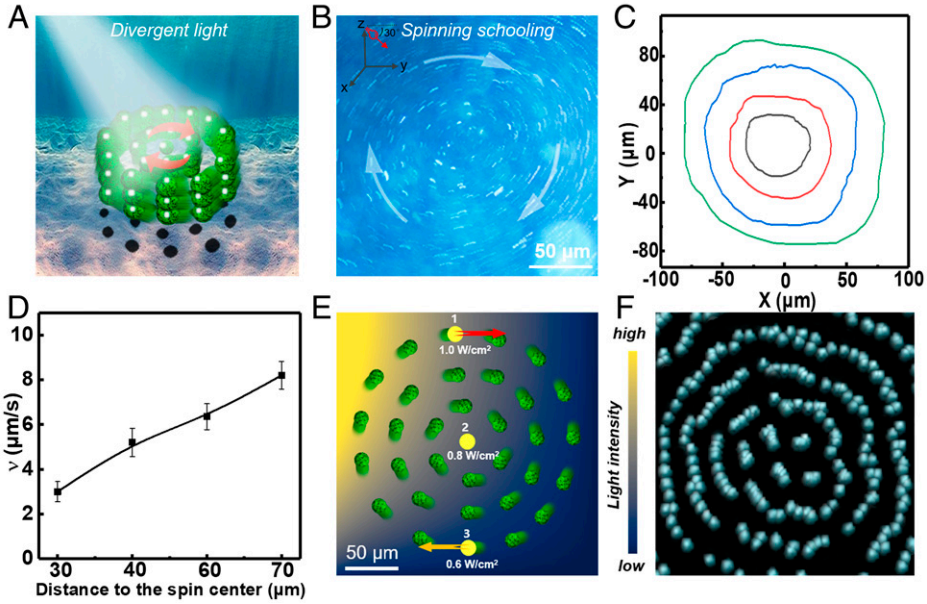

Fig. 4. (*A*) Schematic illustration showing the collective behavior of a group of the C_3N_4/PPyNP-based MNMs under tilted nonuniform light irradiation with medium intensities (spinning schooling). (*B*) The overlaid optical microscopic image of the spinning schooling motion of the MNMs obtained from Movie S7 (1.0-W/cm^2 light intensity). *Inset* in *B*: The incident light angle (30°). (*C*) The representative trajectories of the four MNMs at the different positions during the spinning schooling motion process and (*D*) the corresponding linear speed of the spinning schooling motion as a function of the distance to the spinning center. (*E*) Schematic showing the local light intensity the MNMs experienced at different positions inside the medium intensity divergent beam of light during the clockwise spinning. (*F*) Simulation snapshot of the spinning vortex of the MNMs inside a medium intensity nonuniform beam.

of PPyNP, this MNM can be propelled by two separate-yet-competitive mechanisms (i.e., self-diffusiophoresis and self-thermophoresis). As a consequence, single-C_3N_4/PPyNP–based MNM can sense the light energy changes and exhibit the biomimetic phototactic behavior in response to light (i.e., positive phototaxis, Brownian-like motion, and negative phototaxis under low, medium, and high irradiation, respectively). So, combining two competitive self-phoresis mechanisms, which is especially suitable for designing active colloids, opens up an additional dimension to realize the MNMs with sophisticated functions, which is unattainable based on single propulsion mechanism. More interestingly, by dynamically changing the light intensity, the MNM experiences a reciprocating motion, and under a finely tuned nonuniform beam, a group of MNMs exhibit a unique spinning schooling behavior. The simple control strategy, the fuel-free nature, together with the light energy–dependent motion behavior of the present MNM, thus pave the way toward the further development of advanced artificial counterpart of the phototactic microorganism for diverse applications.

Materials and Methods

Materials. Urea, methanol, PVA, iron chloride, and Span 80 were purchased from Sigma Aldrich Inc. Pyrrole, gelatin, paraffin, glutaraldehyde, acetone, and carbon tetrachloride were obtained from J&K chemicals. The proton indicator (pyranine) was obtained from J&K Scientific. PS microspheres (diameter: 1 μm) were purchased from Aladdin Chemistry Co. Ltd. Green algae (*Chlorella vulgaris*) was purchased from Guibo Company.

Synthesis of C_3N_4 Nanosheets. A total of 10 g urea was calcined in a muffle furnace at 550 °C for 2 h. The temperature was ramped up and down at a rate of 5 °C/min for both heating and cooling. The resulting C_3N_4 was delaminated by the ultrasonication in methanol for 5 h. The C_3N_4 nanosheet was obtained after the evaporation of methanol.

Synthesis of PPyNP. A total of 0.75 g PVA was dissolved in 10 mL deionized water at 60 °C under stirring. After cooling down to room temperature, 0.63 g $FeCl_3$ was added. A total of 100 μL pyrrole was then dropped into the above solution placed in an ice bath. The solution was allowed to react for 24 h at 5 °C, which was then centrifuged at 13,000 rpm three times to remove the excess reactants and dried to obtain PPyNPs.

Preparation of the C_3N_4/PPyNP-Based MNM. On the one hand, 0.3 g gelatin was dissolved in 10 mL deionized water upon heating. A 0.7-g C_3N_4 and PPyNP mixture (1:1) was then added into the cooled gelatin solution and agitated to obtain a homogeneous solution. On the other hand, 0.5 g Span 80 was added to 30 mL liquid paraffin. Then, 1 mL gelatin aqueous solution containing C_3N_4/PPyNP was then added into 30 mL paraffin placed in the ice bath and emulsified at 900 rpm for 10 min. A total of 20 μL glutaraldehyde (1 wt%) were then added to crosslink gelatin in the resulting microparticles. The resulting solution was then centrifuged at 8,000 rpm and washed by acetone and carbon tetrachloride solvents for three times to obtain the MNM. The MNMs were finally dispersed in 1 mL water.

Preparation of the PPyNP/PVA- and C_3N_4/PtNP-Based MNM. The synthesis of the PPy/PVA- and PPy/PtNP-based MNMs followed the same protocol as that of the C_3N_4/PPyNP-based MNM except that the PPyNP/PVA or C_3N_4/PtNP was utilized instead of C_3N_4/PPyNP, respectively.

Characterizations. Scanning electron microscope (SEM) image and the corresponding energy dispersive X-ray spectroscopy (EDX) analysis were obtained on a Zeiss Supra55 scanning electron microscope. For the MNM study, a customized liquid sample container containing the MNM solution was placed on the sample stage and observed under the NIKON Ti-S optical microscope. The movement of the MNM under light irradiation was realized by applying a Model X-Cite 120Q mercury lamp with tunable on/off and intensities, which was placed 1 cm away from the MNM solution. The motion behaviors of the single MNM (1.5×10^2/μL) and a group of MNMs (2×10^5/μL) were observed and recorded at 25 frames per second (fps). For the macroscopic collective phototaxis, 1 mg C_3N_4/PPyNP-based MNM was first dispersed in 2 mL water in a cuvette, which was then illuminated by the light source with different intensities. EPR measurement was carried out on a BRUKER EMXPlus instrument. Image J and MATLAB software were utilized to analyze the motion speed and the trajectory of the MNM. UV-Vis-NIR spectra were acquired on a PerkinElmer Lambda 750 spectrophotometer. The thermogravimetric analysis (TGA) was conducted by a METTLER TOLEDO TGA1 instrument. The Fourier transform infrared spectroscopy (FTIR) spectrum was obtained on a Bruker HYPERION spectrometer. The photo generated current was measured by a KEITHLEY 4200-SCS semiconductor characterization system. Time-resolved photoluminescence spectra were recorded with a FluoroMax-4 spectrofluorometer (HORIBA Scientific). The zeta potential data of the MNM were measured by Particle Size & Zeta Potential Analyzer (Model ZEN3590, Nano ZS90). The solution temperatures of the exposed and unexposed areas were recorded by a Fotric 225s infrared camera. In order to monitor the solution pH changes, 200 μL pyranine pH indicator solution (0.1 mM) was added dropwisely to the 2-mL MNM solution prior to the light irradiation.

Data Availability. All data discussed in the paper are available in the main text and *SI Appendix*.

ACKNOWLEDGMENTS. This work was supported by the National Key Research and Development Program of China (Grant 2018YFE0306105), the National Natural Science Foundation of China (Grant Nos. 22173068 and 11874397), and the Collaborative Innovation and the Collaborative Innovation Center of Suzhou Nano Science and Technology. This work was also supported by the Priority Academic Program Development of Jiangsu Higher Education Institutions, the 111 Project, Joint International Research Laboratory of Carbon-Based Functional Materials and Devices, the Fund for Excellent Creative Research Teams of Jiangsu Higher Education Institutions, and by the Strategic Priority Research Program of Chinese Academy of Sciences (Grant XDB33000000).

1. G. Jékely, Evolution of phototaxis. *Philos. Trans. R. Soc. Lond. B Biol. Sci.* **364**, 2795–2808 (2009).
2. G. Jékely *et al.*, Mechanism of phototaxis in marine zooplankton. *Nature* **456**, 395–399 (2008).
3. D. B. Weibel *et al.*, Microoxen: Microorganisms to move microscale loads. *Proc. Natl. Acad. Sci. U.S.A.* **102**, 11963–11967 (2005).
4. I. S. Aranson, Microrobotics: Swimmers by design. *Nature* **531**, 312–313 (2016).
5. C. Lozano, B. Ten Hagen, H. Löwen, C. Bechinger, Phototaxis of synthetic microswimmers in optical landscapes. *Nat. Commun.* **7**, 12828 (2016).
6. S. Palagi *et al.*, Structured light enables biomimetic swimming and versatile locomotion of photoresponsive soft microrobots. *Nat. Mater.* **15**, 647–653 (2016).
7. L. Xu, F. Mou, H. Gong, M. Luo, J. Guan, Light-driven micro/nanomotors: From fundamentals to applications. *Chem. Soc. Rev.* **46**, 6905–6926 (2017).
8. F. Mou *et al.*, Phototactic flocking of photochemical micromotors. *iScience* **19**, 415–424 (2019).
9. H. Šípová-Jungová, D. Andrén, S. Jones, M. Käll, Nanoscale inorganic motors driven by light: Principles, realizations, and opportunities. *Chem. Rev.* **120**, 269–287 (2020).
10. J. Katuri, X. Ma, M. M. Stanton, S. Sánchez, Designing micro and nanoswimmers for specific applications. *Acc. Chem. Res.* **50**, 2–11 (2017).
11. Y. Tu, F. Peng, D. A. Wilson, Motion manipulation of micro and nanomotors. *Adv. Mater.* **29**, 1701970 (2017).
12. S. Giudicatti *et al.*, Photoactive rolled-up TiO_2 microtubes: Fabrication, characterization and applications. *J. Mater. Chem. C* **2**, 5892–5901 (2014).
13. W. Li, X. Wu, H. Qin, Z. Zhao, H. Liu, Light driven and light guided microswimmers. *Adv. Funct. Mater.* **26**, 3164–3171 (2016).
14. E. Uchida, R. Azumi, Y. Norikane, Light-induced crawling of crystals on a glass surface. *Nat. Commun.* **6**, 7310 (2015).
15. Y. Dong, M. Liu, H. Zhang, B. Dong, Reconfigurable OR and XOR logic gates based on dual responsive on-off-on micromotors. *Nanoscale* **8**, 8378–8383 (2016).
16. R. Dong, Q. Zhang, W. Gao, A. Pei, B. Ren, Highly efficient light driven TiO_2−Au Janus micromotor. *ACS Nano* **10**, 839–844 (2016).
17. M. Ibele, T. E. Mallouk, A. Sen, Schooling behavior of light-powered autonomous micromotors in water. *Angew. Chem. Int. Ed.* **48**, 3308–3312 (2009).
18. H. R. Jiang, N. Yoshinaga, M. Sano, Active motion of a Janus particle by self-thermophoresis in a defocused laser beam. *Phys. Rev. Lett.* **105**, 268302 (2010).
19. M. Xuan *et al.*, Near infrared light-powered Janus mesoporous silica nanoparticle motors. *J. Am. Chem. Soc.* **138**, 6492–6497 (2016).
20. H. Choi, G. H. Lee, K. S. Kim, S. K. Hahn, Light-guided nanomotor systems for autonomous photothermal cancer therapy. *ACS Appl. Mater. Interfaces* **10**, 2338–2346 (2018).
21. R. Dong *et al.*, Visible light driven BiOI-based Janus micromotor in pure water. *J. Am. Chem. Soc.* **139**, 1722–1725 (2017).
22. B. Dai *et al.*, Programmable artificial phototactic microswimmer. *Nat. Nanotechnol.* **11**, 1087–1092 (2016).
23. Y. Wu, T. Si, X. Lin, Q. He, Near infrared-modulated propulsion of catalytic Janus polymer multilayer capsule motors. *Chem. Commun.* **51**, 511–514 (2015).

24. C. Chen *et al.*, Light steered isotropic semiconductor micromotors. *Adv. Mater.* **29**, 1603374 (2017).
25. J. Wang, Z. Xiong, J. Zheng, X. Zhan, J. Tang, Light driven micro/nanomotor for promising biomedical tools: Principle, challenge, and prospect. *Acc. Chem. Res.* **51**, 1957–1965 (2018).
26. J. Zheng *et al.*, Orthogonal navigation of multiple visible-light-driven artificial microswimmers. *Nat. Commun.* **8**, 1438 (2017).
27. T. Xu, W. Gao, L. P. Xu, X. Zhang, S. Wang, Fuel-free synthetic micro/nanomachines. *Adv. Mater.* **29**, 1603250 (2017).
28. J. Zheng *et al.*, Full spectrum tunable visible light driven alloy nanomotor. *Adv. Funct. Mater.* **29**, 1901768 (2019).
29. S. Du, H. Wang, C. Zhou, W. Wang, Z. Zhang, Motor and rotor in one: Light-active ZnO/Au twinned rods of tunable motion modes. *J. Am. Chem. Soc.* **142**, 2213–2217 (2020).
30. M. Xuan *et al.*, Self-propelled nanomotors for thermomechanically percolating cell membranes. *Angew. Chem. Int. Ed.* **57**, 12463–12467 (2018).
31. J. Palacci, S. Sacanna, A. P. Steinberg, D. J. Pine, P. M. Chaikin, Living crystals of light-activated colloidal surfers. *Science* **339**, 936–940 (2013).
32. J. Tong *et al.*, Visible light driven water-fueled ecofriendly micromotors based on iron phthalocyanine for highly efficient organic pollutant degradation. *Langmuir* **36**, 6930–6937 (2020).
33. D. Zhang *et al.*, A phototactic liquid micromotor. *J. Mater. Chem. C* **6**, 12234 (2018).
34. X. Chen, C. Zhou, W. Wang, Colloidal motors 101: A beginner's guide to colloidal motor research. *Chem. Asian J.* **14**, 2388–2405 (2019).
35. Y. Zheng *et al.*, Nanoporous graphitic-C_3N_4@carbon metal-free electrocatalysts for highly efficient oxygen reduction. *J. Am. Chem. Soc.* **133**, 20116–20119 (2011).
36. F. Zhao *et al.*, Highly efficient solar vapour generation via hierarchically nanostructured gels. *Nat. Nanotechnol.* **13**, 489–495 (2018).
37. H. C. Kang, K. E. Geckeler, Enhanced electrical conductivity of polypyrrole prepared by chemical oxidative polymerization: Effect of the preparation technique and polymer additive. *Polymer* **41**, 6931–6934 (2000).
38. Y. Hong, M. Diaz, U. M. Cordova-Figueroa, A. Sen, Light driven titanium-dioxide-based reversible microfireworks and micromotor/micropump systems. *Adv. Funct. Mater.* **20**, 1568–1576 (2010).
39. A. T. Brown, W. C. Poon, C. Holm, J. de Graaf, Ionic screening and dissociation are crucial for understanding chemical self-propulsion in polar solvents. *Soft Matter* **13**, 1200–1222 (2017).
40. A. Brown, W. Poon, Ionic effects in self-propelled Pt-coated Janus swimmers. *Soft Matter* **10**, 4016–4027 (2014).
41. Y. Zhou *et al.*, Radiotherapy-sensitized tumor photothermal ablation using γ-polyglutamic acid nanogels loaded with polypyrrole. *Biomacromolecules* **19**, 2034–2042 (2018).
42. S. Merabia, S. Shenogin, L. Joly, P. Keblinski, J. L. Barrat, Heat transfer from nanoparticles: A corresponding state analysis. *Proc. Natl. Acad. Sci. U.S.A.* **106**, 15113–15118 (2009).
43. Y. Yang *et al.*, Fe_3O_4@MnO_2@PPy nanocomposites overcome hypoxia: Magnetic-targeting-assisted controlled chemotherapy and enhanced photodynamic/photothermal therapy. *J. Mater. Chem. B* **6**, 6848–6857 (2018).
44. G. Zhao, M. Viehrig, M. Pumera, Challenges of the movement of catalytic micromotors in blood. *Lab Chip* **13**, 1930–1936 (2013).
45. J. Liu *et al.*, Water splitting. Metal-free efficient photocatalyst for stable visible water splitting via a two-electron pathway. *Science* **347**, 970–974 (2015).